

Sensors & Diagnostics

Accepted Manuscript

This article can be cited before page numbers have been issued, to do this please use: V. Ankalgi, M. A. Belgami, K. Bhakti, S. M. Jeong and C. S. Rout, *Sens. Diagn.*, 2025, DOI: 10.1039/D5SD00187K.



This is an Accepted Manuscript, which has been through the Royal Society of Chemistry peer review process and has been accepted for publication.

Accepted Manuscripts are published online shortly after acceptance, before technical editing, formatting and proof reading. Using this free service, authors can make their results available to the community, in citable form, before we publish the edited article. We will replace this Accepted Manuscript with the edited and formatted Advance Article as soon as it is available.

You can find more information about Accepted Manuscripts in the [Information for Authors](#).

Please note that technical editing may introduce minor changes to the text and/or graphics, which may alter content. The journal's standard [Terms & Conditions](#) and the [Ethical guidelines](#) still apply. In no event shall the Royal Society of Chemistry be held responsible for any errors or omissions in this Accepted Manuscript or any consequences arising from the use of any information it contains.

ARTICLE

MXene-Supported Cu-Ag Nanohybrids for Electrochemical Nitrate and Nitrite Detection in Alkaline MediaVishwanath Ankalgi^a, Mohammed Arkham Belgami^a, Bhakti Kulkarni^a, Sang Mun Jeong^{b*}, Chandra Sekhar Rout^{a,b*}Received
Accepted

DOI:

In this study, an electrochemical sensor based on $\text{Ti}_3\text{C}_2\text{T}_x$ MXene functionalized with bimetallic Cu-Ag nanoparticles was developed for the selective and sensitive detection of nitrate and nitrite ions. Owing to the high surface area, excellent conductivity, and versatile surface chemistry of $\text{Ti}_3\text{C}_2\text{T}_x$, the sensor exhibits dual linear response ranges for nitrate (0.1–10 mM and 10–100 mM), while enabling simultaneous nitrite detection across the same concentration intervals of nitrate addition. The detection limits for nitrate were calculated as 5.2 μM and 124.0 μM , with corresponding sensitivities of 220.75 and 5.095 $\mu\text{A mM}^{-1} \text{cm}^{-2}$, and for nitrite (0.1–1 mM and 1–30 mM), the detection limits calculated for nitrite were 0.031 μM and 0.211 μM with sensitivities of 898.12 and 131.35 $\mu\text{A mM}^{-1} \text{cm}^{-2}$, respectively. The sensor further demonstrates remarkable selectivity against common interfering species and retains electrochemical stability over 100 cyclic voltammetry cycles. Validation through real-sample analysis in soil, lake water, and tap water yielded high recovery rates, underscoring its practical utility. Overall, this study highlights the successful deployment of MXene-based electrochemical sensing for nitrate and nitrite ions, extending the scope of MXene applications beyond conventional reduction processes.

1. Introduction

In recent decades, the pollution of water supplies by industrial and agricultural activities has emerged as a significant global problem. Water pollution encompasses a wide range of chemical, biological, and physical contaminants that compromise aquatic ecosystems and human health.¹ In addition to nitrogen-based species like nitrates and nitrites, common pollutants include heavy metals (e.g., Pb, Hg, Cd), organic compounds (e.g., pesticides, pharmaceuticals), and microbial pathogens.² These substances can originate from industrial effluents, agricultural runoff, and domestic waste, and often persist in the environment, leading to bioaccumulation and chronic toxicity. Among the various water and soil contaminants, the substances most incriminated are surely nitrate ions (NO_3^-).³ In the food industry, NO_3^- ions are used extensively not only in fertilizers but also as an addition to improve color and flavor or as a preventative measure against *Clostridium botulinum* food poisoning.⁴ Nitrite ions (NO_2^-) are a widespread contaminant in agricultural runoff and industrial effluents, similar to NO_3^- . It poses significant health risks due to its ability to form carcinogenic nitrosamines and interfere with

oxygen transport in the bloodstream. Regulatory agencies have set strict limits for NO_2^- concentrations in drinking water, necessitating a sensitive and selective detection method. Nevertheless, a high concentration of NO_3^- has several negative consequences for human health, as it can be transformed into toxic nitrogen compounds, including NO_2^- , nitric oxide, and N-nitrosamines, which can lead to liver disease and stomach cancer.⁵ Blue baby syndrome, usually referred to as neonatal methemoglobinemia, is likewise caused by an excessive consumption of NO_3^- .⁶ The World Health Organization (WHO) and European Directives have set the maximum contamination level (MCL) of NO_3^- in public drinking water at 50 mg/L (about 0.8 mM) due to its harmful effects on human health. Determining the proper levels of NO_3^- , particularly in drinking water, is therefore crucial. Traditional methods for NO_3^- and NO_2^- detection include spectrophotometry, ion chromatography, and GC-MS, each offering distinct advantages in terms of sensitivity and specificity. However, these techniques often require complex instrumentation and sample preparation.^{7,8} Recent developments in electrochemical sensing, especially those leveraging nanomaterials have enabled portable, low-cost, and highly sensitive platforms for real-time monitoring.

The detection of nitrogenous pollutants such as NO_3^- and NO_2^- is of growing importance due to their environmental and health implications. Transition metals like copper (Cu), titanium (Ti), and silver (Ag) offer distinct advantages in electrochemical sensing platforms owing to their unique physicochemical properties. Cu exhibits excellent redox activity and facilitates electron transfer, Ti provides structural stability and photocatalytic potential, while Ag enhances electrical

^a Centre for Nano and Material Science, Jain University, Jain global campus, Jakkasandra, Ramanagaram, Bangalore - 562112, India.

^b Department of Chemical Engineering, Chungbuk National University, Cheongju, Chungbuk 28644, Republic of Korea.

^c Advanced Energy Research Institute, Chungbuk National University, Cheongju, Chungbuk 28644, Republic of Korea.

*Corresponding author: csrout@gmail.com, r.chandrasekhar@jainuniversity.ac.in (CSR); smjeong@chungbuk.ac.kr (SMJ)

Electronic Supplementary Information (ESI) available: [details of any supplementary information available should be included here]



conductivity and signal amplification.^{9,10} Recent studies have shown that doping Ti-based frameworks with Cu and Ag not only narrows the bandgap but also improves charge separation and catalytic efficiency, thereby enabling sensitive and selective detection of nitrogenous species. Bagheri et al. developed an electrochemical sensor based on a composite of Cu nanoparticles (NPs), multi-walled carbon nanotubes, and reduced graphene oxide for NO_3^- detection, achieving a low limit of detection (LOD) of 20 nM. However, the sensor exhibited a relatively narrow linear range and required electrodeposition for sample preparation to enable simultaneous NO_2^- detection.¹¹ Inam et al. reported a flexible screen-printed electrochemical sensor functionalized with electrodeposited Cu NPs on an Ag screen-printed electrode, achieving an impressive LOD of 0.12 $\mu\text{g/L}$ and a linear dynamic range (LDR) of 0.05–5 mM.¹² Ankush et al. introduced a polyvinyl alcohol/copper–nickel co-doped titania (PCNT) nanocomposite sensor, which demonstrated an LOD of 204.71 μM and a limit of quantification (LOQ) of 620.34 μM .¹³ More recently, Saad et al. fabricated a highly sensitive NO_3^- sensor using a hybrid film of poly(1,8-diaminonaphthalene) and Cu oxide particles, achieving an LOD of 0.5 μM with a linear range of 2–200 μM .¹⁴ While these studies demonstrate significant progress in electrochemical NO_3^- sensing, many involve complex fabrication steps, limited linear ranges, or require rigid substrates and specialized deposition techniques. To reduce NO_3^- and NO_2^- , recent studies have investigated various metal catalysts, including Cu, gold (Au), and Ag, which do not require sophisticated biorecognition elements like enzymes.^{12,15,16} When compared to other metal catalysts, Cu has shown better performance as an electro-reduced catalyst for NO_3^- ion detection due to its high conductivity ($5.8 \times 10^7 \text{ S/m}$). The combination of Ag and Cu reduces NO_3^- in environmental samples in a selective manner while limiting interference from other competing species. Ag NPs assist in reducing undesirable side reactions and improve NO_3^- selectivity over other anions by facilitating regulated adsorption-desorption behavior. The synergistic interaction between Ag and Cu plays a pivotal role in enhancing the electrochemical sensing of NO_3^- and NO_2^- . Specifically, the presence of Ag NPs modulates the reduction potential of NO_3^- , enabling efficient detection at lower applied voltages. This shift leads to an improved signal-to-noise ratio, thereby lowering the detection limit and enhancing overall analytical performance. Cu-based sensors integrated with Ag NPs exhibit superior stability, selectivity, and catalytic activity, along with accelerated electron transfer kinetics. The bimetallic synergy between Ag and Cu thus creates a robust sensing interface capable of high-performance NO_3^- detection in both industrial and environmental settings.^{17,18}

Recent advances in MXene-based electrochemical sensors have demonstrated that surface modification with metals and carbonaceous materials can dramatically enhance sensing performance. For example, $\text{Ti}_3\text{C}_2\text{T}_x$ modified with Au NPs showed superior catalytic activity and stability for hydrogen evolution reactions.¹⁹ Complementing the metal-based enhancements, MXenes and their hybrid derivatives offer a highly favorable platform for sensor fabrication due to their

exceptional physicochemical properties. MXenes exhibit high electrical conductivity, a large specific surface area, and tunable surface terminations ($-\text{OH}$, $-\text{O}$, $-\text{F}$), which facilitate functionalization and enhance analyte interaction.²⁰ These features help overcome common limitations in conventional sensor devices. MXene NPs serve as excellent modifiers in electrochemical sensor design, enabling enhanced sensitivity and selectivity. Their layered, atomically thin structure supports efficient ion intercalation and charge transfer, while their quantum confinement effects and nontoxic nature further contribute to sensor reliability. Beyond sensing, MXenes have demonstrated versatility across various applications, including supercapacitors, fuel cells, gas sensors, biosensors, water purification, and catalysis, underscoring their potential as next-generation transducer materials.²¹ In contrast, the present work emerges as a highly efficient and reliable platform, highlighting the previously underexplored potential of MXene as a functional matrix for electrochemical NO_3^- and NO_2^- sensing using a $\text{Ti}_3\text{C}_2\text{T}_x$ MXene matrix uniformly decorated with Cu-Ag NPs on a disposable carbon electrode strip. This platform not only simplifies sensor fabrication by eliminating the need for electrodeposition or polymeric binders but also achieves competitive sensitivity, a broader linear dynamic range, and excellent selectivity. This study demonstrates the use of MXene as a functional matrix for electrochemical NO_3^- detection, marking a significant advancement in the development of facile, scalable, and high-performance sensors for real-world environmental monitoring.

2. Experimental

2.1. Materials

For the synthesis of $\text{Ti}_3\text{C}_2\text{T}_x$ MXene matrix uniformly decorated with Cu-Ag NPs (TCX-AgCu), a simple chemical reduction method is employed, without further alteration; all analytical-grade compounds were used for the synthesis. Titanium aluminum carbide (Ti_3AlC_2 , Y-Carbon Ltd., Ukraine), lithium fluoride (LiF, 99.5%, HIMEDIA), silver nitrate (AgNO_3 , 99%, LOBA Chemie), cupric chloride (CuCl_2 , 99%, LOBA Chemie), sodium sulfate (Na_2SO_4 , 99%, SRL), sodium nitrate (NaNO_3 , 99%, EMPLURA), sodium nitrite (NaNO_2 , 99%, EMPLURA), sodium borohydride (NaBH_4 , 98%, SRL), potassium chloride (KCl, 99.5%, SDFCL), ammonium acetate ($\text{CH}_3\text{COONH}_4$, 98%, EMPLURA), manganese sulfate (MnSO_4 , 98%, EMPLURA), potassium ferrocyanide ($\text{K}_4[\text{Fe}(\text{CN})_6]$, 99%, SRL), potassium ferricyanide ($\text{K}_3[\text{Fe}(\text{CN})_6]$, 98%, SRL), ferrous sulfate (FeSO_4 , 99.5%, EMPLURA), ferric chloride (FeCl_3 , 98%, SDFCL), hydrochloric acid (HCl, 37%, SDFCL), sulfuric acid (H_2SO_4 , analytical grade), and isopropyl alcohol ($\text{C}_3\text{H}_8\text{O}$, 99%, MERCK), Metrohm dropsens SPCE 110 (Screen printed carbon electrode), Palmsens SPE connector (2mm banana), and distilled water.

2.2. MXene Etching Procedure

Adopting the HCl/LiF method for etching the Ti_3AlC_2 MAX phase to the $\text{Ti}_3\text{C}_2\text{T}_x$ MXene phase (TCX), 15 ml of 37% HCl + 5 ml H_2O is added to 1.2g of LiF and 1 g of well-ground Ti_3AlC_2 MAX phase, stirred well, and maintained at the optimum temperature of 50 $^\circ\text{C}$ for 48 hours. The etched TCX is filtered



and washed with deionized (DI) water and ethanol until a pH of 7 is achieved. It is kept drying in a vacuum oven (60 °C) for 24 hours.

2.3. Synthesis of TCX-AgCu Composite

Disperse TCX in 10 mL ethanol/water via ultrasonication. Prepare aqueous solutions of AgNO_3 and CuCl_2 at a concentration of 1 mM. Add 1 mL of each metal solution to the MXene dispersion. Add 5 mL of newly made ice-cold NaBH_4 (0.01 M) dropwise and mix. Stir for 1 hour at 0–5°C, then centrifuge and wash. Dry or scatter the TCX-AgCu hybrid in ethanol. The sample was centrifuged, filtered using ethanol and DI water, and then dried in a vacuum oven. The precursor remained constant throughout, while TCX was added to the solution at varying quantities (5, 25, 50, and 75 mg and denoted as 5TCX-AgCu, 25TCX-AgCu, 50TCX-AgCu and 75TCX-AgCu) **Figure 1** illustrates the synthesis of TCX-AgCu.

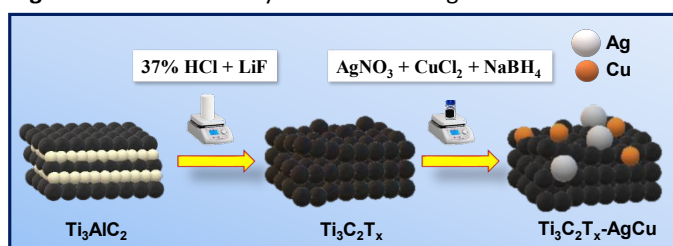


Figure 1: Schematic illustration depicting the synthesis route of TCX-AgCu;

2.4. Material Characterization

X-ray diffraction (XRD) using $\text{CuK}\alpha$ radiation with a wavelength of approximately 0.154 nm was employed to assess the phase purity and crystallinity of the material within the 2θ range of 10–80°, at a scan rate of 1° min^{-1} (Rigaku Ultima IV X-ray diffractometer, Rigaku Company, Japan). The internal structure, surface morphology, and elemental composition were analyzed using field emission scanning electron microscopy (FESEM, using JEOL JSM 7100F, JEOL Ltd.) (CNMS, Jain University), transmission electron microscopy (TEM; JEM-2100F, UHR, JEOL, KBSI), and energy-dispersive X-ray spectroscopy (EDS). X-ray photoelectron spectroscopy (XPS; PHI Quantera-II, Al $\text{K}\alpha$ radiation, Ulvac-PHI) was utilized to investigate the valence states of the elements and near-surface elemental compositions (Chungbuk National University). The nanocomposite was synthesized using an Elmasonic EASY ultrasonic cleaner.

2.5. Surface Modification and Electrochemical Characterization

Surface modification of electrodes plays a pivotal role in tuning electrochemical behavior, as it directly influences charge transfer dynamics and analyte interaction. As discussed by Sterin et al. (2024), various chemical strategies have been employed to functionalize electrode surfaces for improved sensing performance.²² The glassy carbon electrode (GCE) was initially polished using a microcloth and an aqueous suspension of 0.05 μm alumina to attain a smooth, mirror-like finish. Following this, 10 μL of 10 mg/mL TCX-AgCu catalyst ink was

drop-cast onto the cleaned GCE surface and subsequently dried at room temperature. For comparison, electrodes modified with only TCX were fabricated using the same procedure. The screen-printed carbon electrode (SPCE) was cleaned with absolute ethanol, dried, and subsequently modified by drop-casting, following the same procedure used for the GCE. All the electrochemical data is obtained via a CorrTest CS2350 workstation in Wuhan, China, electrochemical characterizations of produced electrodes, including Cyclic voltammetry (CV), Square-wave voltammetry (SWV), and Electrochemical impedance spectroscopy (EIS), have been performed. Using a sinusoidal potential of 5 mV and a frequency range of 0.01 Hz to 100 kHz.

3. Results and Discussion

3.1. Structural and Compositional Characterization of 5TCX-AgCu:

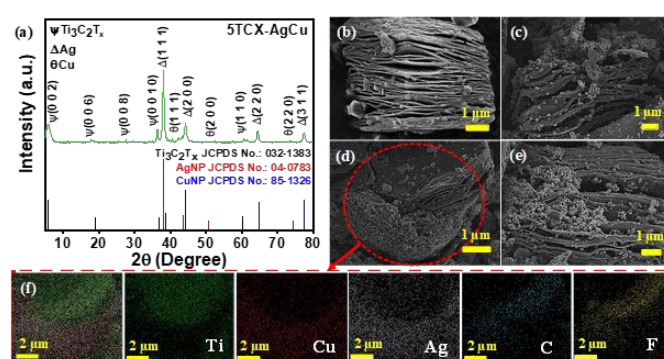


Figure 2: (a) XRD pattern; FESEM images of (b) TCX, (c-e) 5TCX-AgCu at 1 μm magnification; (f) EDAX analysis confirming elemental composition of 5TCX-AgCu at 2 μm magnification.

To comprehensively investigate its physicochemical characteristics, the material was subjected to a series of advanced characterization techniques. X-ray diffraction (XRD) analysis confirmed the successful incorporation of Ag and Cu NPs within the TCX framework, referencing **Figure 2a**. Distinct diffraction peaks observed at 2θ values of 38.18°, 44.25°, 64.72°, and 77.40° correspond to the (111), (200), (220), and (311) planes of face-centered cubic (fcc) Ag (JCPDS No. 04-0783). Similarly, peaks at 43.7°, 50.7°, and 74.3° were assigned to the (111), (200), and (220) planes of fcc Cu (JCPDS No. 85-1326). The characteristic peaks at 5.8°, 19.1°, 34.0°, 38.8°, and 60.2° are consistent with the (002), (006), (008), (0010), and (110) planes of TCX (JCPDS No. 032-1383), indicating the preservation of the layered structure. Notably, when compared with the XRD of TCX (**Figure S1**), the primary (002) peak observed at $2\theta \approx 9.5^\circ$, corresponding to a d-spacing of $\sim 9.3 \text{ \AA}$, shifts toward lower angles ($\approx 5.8^\circ$), indicating an expanded interlayer spacing ($\sim 15.2 \text{ \AA}$), which is attributed to intercalation or hydration effects during synthesis. According to **Figure 2b**, field emission scanning electron microscopy (FESEM) images reveal the characteristic stacked morphology of TCX, along



with surface functionalization indicative of successful etching of Al from the Ti_3AlC_2 precursor. The negatively charged TCX surface facilitates the electrostatic deposition of positively charged Cu^{2+} and Ag^+ ions, resulting in uniform decoration with Cu and Ag NPs, as shown in **Figure 2(c-e)**. While energy-dispersive X-ray spectroscopy (EDS) elemental mapping highlights discrete Ag signals and uniformly dispersed Cu, corroborating the presence of distinct metallic species as revealed in **Figure 2f**.

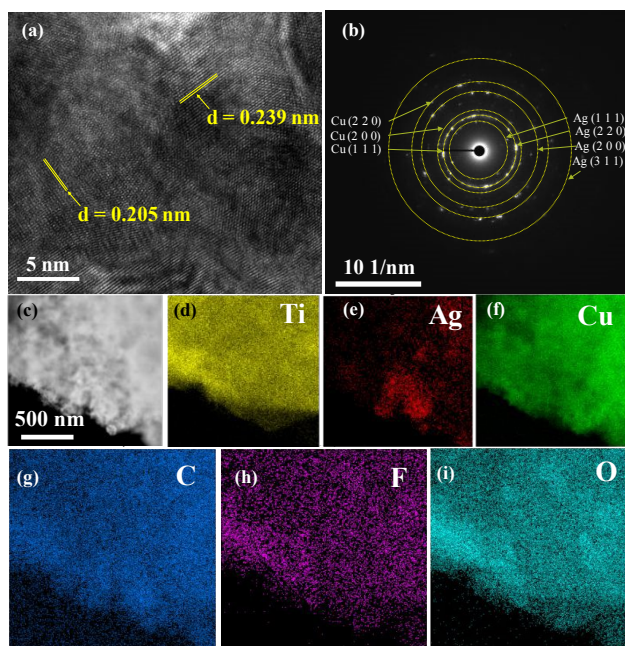


Figure 3: (a) HRTEM image, (b) SAED, (c)-(i) TEM image and element mapping of 5TCX-AgCu.

Transmission electron microscopy (TEM) further confirms the homogeneous distribution of NPs across the TCX surface (**Figure 3**). As demonstrated in **Figure 3a**, high-resolution transmission electron microscopy (HRTEM) analysis provides further structural insights. Lattice fringes with interplanar spacing's of 0.239 nm were attributed to the (111) plane of fcc Ag, respectively, confirming the crystalline nature of the Ag NPs. Furthermore, nanoclusters measuring approximately 3-5 nm in proximity to Ag NPs displayed a lattice spacing of 0.205 nm, consistent with the (111) crystallographic plane of fcc Cu. This observation was corroborated through particle size comparison studies (**Table S1**). Importantly, no evidence of Cu-Ag alloy formation was observed, suggesting independent nucleation and growth of Ag and Cu on the TCX surface. This behavior is likely driven by strong interactions between the abundant surface terminations (-F and -OH) of TCX and the metal precursors, promoting selective nucleation and spatial separation of Ag and Cu species with Ti, C, OH, and F, as evidenced by the TEM imagery and corresponding elemental mapping shown in **Figure 3(c-i)**. The selected area electron diffraction (SAED) patterns presented in **Figure 3b** reveal distinct lattice fringes with

interplanar spacing's corresponding to the fcc phases of Cu and Ag, which are consistent with the diffraction peaks observed in the XRD analysis. Inductively Coupled Plasma (ICP) spectroscopy was employed to quantitatively assess the elemental composition of the 5TCX-AgCu material. As a highly sensitive and precise technique, ICP enables accurate determination of the actual loading of metallic species. The analysis confirmed the successful incorporation of Ag and Cu into the TCX matrix, yielding loadings of approximately 52.20 wt% for Ag and 26.86 wt% for Cu. These values are in close agreement with the targeted synthesis ratios, thereby validating the effectiveness of the loading strategy (**Table S1**).

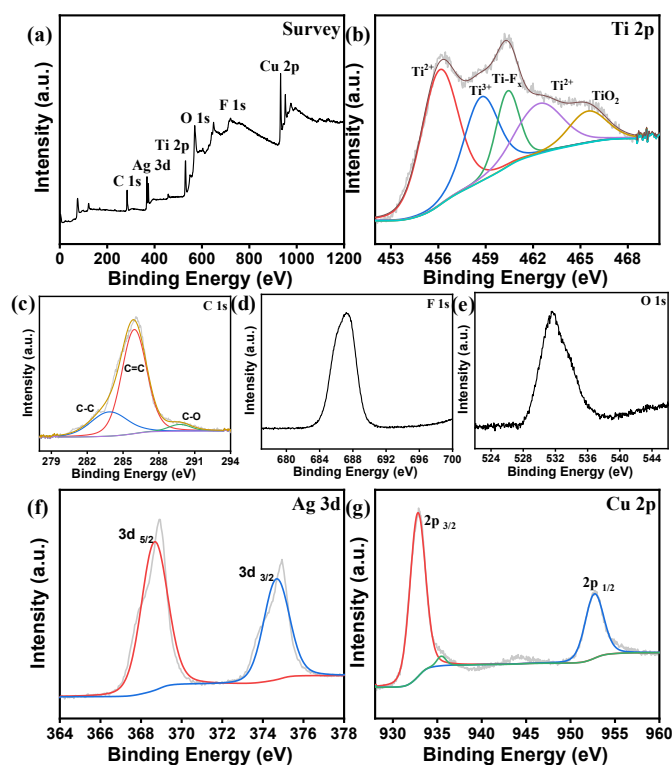


Figure 4: (a) XPS survey spectrum, XPS spectra of (b) Ti 2p, (c) C 1s, (d) F 1s, (e) O 1s, (f) Ag 3d and (g) Cu 2p of 5TCX-AgCu.

X-ray photoelectron spectroscopy (XPS) was employed to elucidate the surface chemistry and electronic structure of the 5TCX-AgCu composite. The survey spectrum (**Figure 4a**) confirmed the presence of Ti, (Titanium), C (Carbon), F (Flourine), Ag, and Cu. The XPS analysis also revealed Ag $3d_{5/2}$ and Ag $3d_{3/2}$ peaks at 368.2 eV and 374.2 eV, respectively, consistent with metallic Ag^0 (**Figure 4f**). The Cu $2p_{3/2}$ peak at ~934.5 eV, and Cu $2p_{1/2}$ peaks at ~952.5 eV, along with shake-up satellites at ~942 eV, confirm the presence of Cu^{2+} species, in agreement with indicating enhanced electrochemical activity due to redox-active Cu sites (**Figure 4g**). The spatially isolated distribution of Ag and Cu NPs, along with the presence of electronegative -F and -OH terminations on the TCX surface, suggests a possible charge transfer from the metal nanoparticles to



the TCX substrate through C interactions (**Figure 4c, d, & e**). This electronic interaction results in the partial oxidation of Ag and Cu, forming $\text{Ag}^{\delta+}$ and $\text{Cu}^{\delta+}$ species, which are believed to enhance the electrocatalytic activity toward NO_3^- and NO_2^- reduction. The Ti 2p spectrum (**Figure 4b**), upon deconvolution, exhibited multiple oxidation states including Ti-F_x , TiO_2 , Ti^{2+} , and Ti^{3+} , confirming the mixed-valent nature of titanium in the composite and the presence of surface functional groups critical for catalytic function. TCX was synthesized via a minimally intensive etching route using HCl and LiF, which typically yields -F, -OH, and -O surface terminations. Although Cl⁻ is present in the etching medium, thorough washing and centrifugation effectively removed residual Cl species. XPS analysis showed no detectable Cl 2p signal, indicating the absence (or sub-detection presence) of Cl terminations. This aligns with prior reports that Cl terminations are thermodynamically unstable and are readily replaced by more favorable groups during aqueous processing.²³

3.2. Electrochemical Studies

3.2.1 Optimization of Electrochemical Conditions for Sensitive Detection:

To achieve optimal sensitivity for NO_3^- and NO_2^- detection, a systematic optimization of the electrochemical system was undertaken, focusing on the selection of a suitable electrolyte and conditioning the electrode material to enhance its electroreductive performance. Initially, various electrolyte systems and material compositions were evaluated to determine the best-performing combination with the modified electrode. Among five different composite formulations, namely 75TCX-AgCu, 50TCX-AgCu, 25TCX-AgCu, and 5TCX-AgCu. The 5TCX-AgCu variant exhibited superior performance, attributed to its enhanced conductivity and uniform dispersion of Ag and Cu NPs (**Figure S2b**). For all GCE and SPCE investigations, a consistent mass loading of 10 mg/mL was maintained (**Figure S2a**), and the optimal accumulation time for NO_3^- detection was established as 30 seconds. Preliminary optimization studies, including screening of all electrolytes and compositions, were conducted using the GCE platform to assess the electrochemical response toward NO_3^- . Among the tested electrolytes, 0.1 M Sodium Sulphate (Na_2SO_4 , pH 7.0), 0.1 M Potassium Chloride (KCl, pH 7.0), and 0.1 M Phosphate Buffer Solution (PBS, pH 7.0), Na_2SO_4 provided the highest peak current response in the presence of 20 mM NO_3^- , denoted by responses 1.372, 0.842, and 0.635 mA for Na_2SO_4 , KCl, and PBS, respectively (**Figure S2b**). Based on these findings, 0.1 M Na_2SO_4 was selected as the supporting electrolyte for further studies. Subsequent pH-dependent experiments, as shown in **Figure S2c**, and **S2d** revealed that the modified electrode exhibited the most pronounced electrocatalytic activity under alkaline conditions (pH 11.0) attained with the required addition of 1M NaOH solution. CV was employed to investigate the redox behavior of NO_3^- on bare and modified electrodes at a scan rate of 50 mV s^{-1} in 0.1 M Na_2SO_4 containing 10 mM NO_3^- . The comparative study using bare GCE, GCE/TCX, and 5TCX-AgCu

modified GCE demonstrated a progressive increase in cathodic peak current (I_{pc}), as illustrated in **Figure S3a**. The bare GCE exhibited a relatively low I_{pc} (-0.190 mA), indicative of poor electron transfer efficiency. Contrasted to the TCX-modified electrode exhibited enhanced electrocatalytic activity, with a I_{pc} of -0.327 mA, due to the improved conductivity and surface reactivity of TCX. Notably, the GCE/5TCX-AgCu electrode delivered the highest I_{pc} (-6.508 mA), highlighting the synergistic effect of Cu and Ag NPs in facilitating NO_3^- and NO_2^- reduction. To further assess the reliability and precision of the electrode, concentration-dependent studies were performed using CV over a potential window ranging from 0 V to -1.3 V. As illustrated in (**Figure 5a**), the forward CV scan reveals four distinct electrochemical events (E1-E4), corresponding to sequential reduction processes. The reverse scan displays additional redox peaks (E5 and E6), indicative of partial reversibility within the system. The initial reduction steps (E1-E3) are predominantly governed by Ag(0) active sites, which facilitate the early-stage electroreduction of NO_3^- . In contrast, Cu(0) sites play a pivotal role in stabilizing intermediate NO_2^- species and promoting their further reduction to ammonia (NH_3) in later stages. These outcomes reveal the synergistic and bifunctional catalytic behavior of the 5TCX-AgCu, enabling a stepwise and efficient transformation of NO_3^- to NH_3 . A similar electrochemical pathway is observed for the SPCE/5TCX-AgCu electrode (**Figure 5b**), where the initial peaks E1 and E2 correspond to the reduction of Cu^{2+} and Ag^+ to their metallic

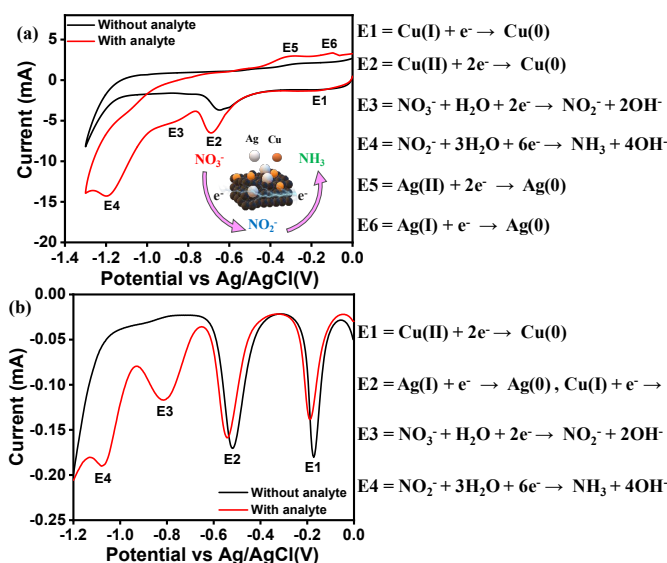
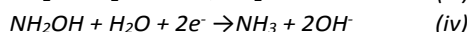
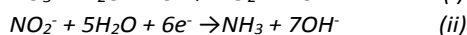


Figure 5: (a) CV profiles of the GCE/5TCX-AgCu electrode in 0.1 M Na_2SO_4 (pH 11.0), recorded in the absence and presence of 10 mM NO_3^- to evaluate analyte response and proposed reaction mechanism, (b) SWV profiles of the SPCE/5TCX-AgCu electrode in 0.1 M Na_2SO_4 (pH 11.0), recorded in the absence and presence of 5 mM NO_3^- to evaluate analyte response and proposed reaction mechanism.

states, which subsequently catalyze the reduction of NO_3^- to NO_2^- (E3), followed by the conversion of NO_2^- to NH_3 (E4).²⁴



The observed response of GCE/5TCX-AgCu is 34.25 times higher than bare, and GCE/TCX is 1.72 times higher than bare (Figure S3a). These results underscore the superior electrocatalytic behavior of the modified electrocatalyst, which demonstrates that 5TCX-AgCu modified SPCE facilitates electron transport more efficiently than SPCE/TCX and SPCE. The TCX provides long-term stability and maintains the dispersion of NPs, which serve as a conductive scaffold for intricate NO_3^- reduction reactions and facilitate electron transfer. While Ag NPs catalyze initial NO_3^- reduction and lower the onset potential, and Cu NPs bind to the intermediates and boost the catalytic current, which helps promote the reduction of NO_2^- to NH_3 . Electrolyte media also play an important role in the sensitivity and selectivity of the target analyte because 0.1 M Na_2SO_4 (pH 11.0) is an alkaline background electrolyte that minimizes migration effect during NO_3^- reduction, and promotes ion mobility while retaining electrochemical stability in the electrode.²⁵ Alkaline conditions maintain NO_3^- stable, reduce the parasitic HER (Hydrogen Evolution Reaction), stabilize the electrode surface, and promote NH_3 production over Nitrogen (N_2).¹⁷ A summary of the general reactions that can occur during the electrocatalytic reduction of NO_3^- in alkaline medium is given by Eqs (i - iv)



A higher density of catalytically active sites leads to improved electrochemical conversion of NO_3^- to detectable products, as Ag NPs alter the electronic structure of Cu NPs, shifting its d-band center and enhancing the adsorption affinity for NO_3^- and its intermediates. The Cu-Ag interface offers bimetallic active sites, which stabilize reaction intermediates and create favorable conditions for NO_3^- reduction. Cu's long-term stability in electrochemical applications may be impacted by its propensity to oxidize and generate CuO or Cu_2O . Ag serves as a protective layer, as it is more resistant to oxidation, which prevents Cu from degrading quickly and keeps the sensor stable over time.^{26,27}

3.2.2. Electrochemical Activity of the Modified Electrode:

The intrinsic charge transfer capability of the synthesized nanomaterials, intended for electrode surface modification, was systematically assessed through a range of electrochemical characterization techniques. CV and EIS are valuable tools for determining oxidation-reduction peak (ORP) current, charge-transfer properties, and diffusion rate on the modified SPCE surface and GCE surface.

The high-frequency semicircular start corresponds to the charge-transfer resistance (R_{ct}), whereas the low-frequency linear area represents the diffusion process. Figure 6b depicts the EIS curves of bare SPCE, SPCE/TCX, and SPCE/5TCX-AgCu measured in Zobel's solution (Equimolar 0.5 mM potassium ferri-ferrocyanide in 0.1M KCl) throughout the frequency range of 100 MHz to 1 kHz. The acquired impedance maps are fitted to a Randel circuit. The Randel circuit yields data for solution

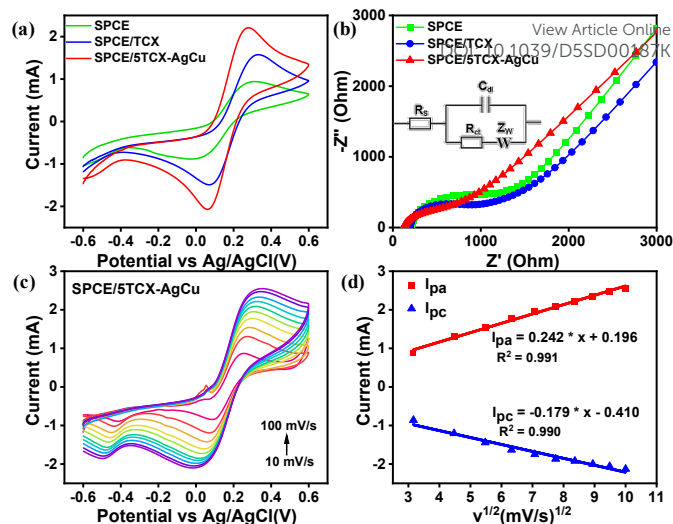


Figure 6: (a) CV comparison of bare SPCE, SPCE/TCX, and SPCE/5TCX-AgCu electrodes; (b) EIS comparison in Zobel's solution for ORP assessment; (c) Scan rate-dependent CV analysis of SPCE/5TCX-AgCu; (d) Corresponding calibration plot for SPCE/5TCX-AgCu.

resistance (R_s), R_{ct} , and double-layer capacitance (C_{dl}). The R_{ct} values for SPCE, SPCE/TCX, and SPCE/5TCX-AgCu are 1007 Ω , 803.6 Ω , and 413 Ω , respectively, which are significantly lower than those when observed for GCE, GCE/TCX, and GCE/5TCX-AgCu (Figure S4b). This highlights the enhanced electron transfer kinetics of the SPCE/5TCX-AgCu configuration. Further, the modified electrode's charge transfer rate constant (k_s) was calculated using equation 1,²⁴

$$R_{ct} = RT / n^2 F^2 k_s C \quad (1)$$

Where R (gas constant = $8.314 \text{ J mol}^{-1} \text{ K}^{-1}$), T (temperature = 25°C), n (number of electrons transferred), F (Faraday constant = $96,485 \text{ C mol}^{-1}$), C (concentration), and k_s (charge transfer rate). According to Equation 1, the calculated k_s for SPCE, SPCE/TCX, and SPCE/5TCX-AgCu are 30.0, 49.5, and 70.3 cm/s , respectively.

Comparative electrochemical studies were performed using TCX individually modified with Ag (5TCX-Ag) and Cu (5TCX-Cu), as well as with both metals simultaneously (5TCX-AgCu). CV conducted in Zobel's solution revealed that while SPCE/5TCX-Ag and SPCE/5TCX-Cu exhibited distinct redox activity, the SPCE/5TCX-AgCu system demonstrated markedly enhanced anodic peak current (I_{pa}) and I_{pc} . This improvement indicates a synergistic effect arising from the co-presence of Ag and Cu, which surpasses the performance achievable by either metal alone (Figure S4c). To further illustrate (Figure 6a), CV analyses were conducted in Zobel's solution to assess the electrochemical characteristics of the three electrodes. Among them, SPCE/5TCX-AgCu exhibited the highest I_{pa} and I_{pc} . Specifically, I_{pa} for SPCE, SPCE/TCX, and SPCE/5TCX-AgCu were 0.94, 1.57, and 2.21 mA, respectively, while the corresponding I_{pc} were -0.88, -1.49, and -2.08 mA. These results confirm that the modified SPCE/5TCX-AgCu electrode delivers the most pronounced current response, indicating superior electrochemical performance that notably surpasses that of GCE, GCE/TCX, and GCE/5TCX-AgCu as illustrated in (Figure



S4a). To further investigate its electrochemical behavior, CV was performed at varying scan rates using SPCE/5TCX-AgCu, as depicted in **Figure 6c**. The data reveal a consistent increase in redox peak currents with increasing scan rate, demonstrating a linear dependence on the square root of the scan rate. This linearity, highlighted in **Figure 6d**, suggests the coexistence of adsorption and diffusion-controlled electron transfer mechanisms.

The electrochemically active surface area (EASA) was determined using Randel's Sevcik equation:²⁸

$$I_p = 2.69 \times 10^5 n^{3/2} A D^{1/2} C v^{1/2} \quad (2)$$

Where I_p is the peak current, n represents the number of transfer electrons, A denotes the surface area of the electrode, D stands for the diffusion coefficient, and C represents the reactant concentration. Based on this analysis, the EASA values were calculated as 387.60 cm² for the unmodified SPCE, 525.22 cm² for the SPCE/TCX, and 690.54 cm² for the SPCE/5TCX-AgCu. These findings suggest that the combination of Ag and Cu NPs with TCX yields the largest EASA values, promoting the electrochemical interaction between the electrode surface and the electrolyte solution. This increased surface area and interaction contribute to the enhanced electrochemical performance, which is evidenced by the highest peak redox currents shown in **Figure 6**. This highlights the superior surface area and electron transfer capabilities of the SPCE/5TCX-AgCu, making it a promising candidate as an electrode active material for electrochemical applications.

3.2.3. Influence of Scanrate:

As **Figure 7b** illustrates the electrochemical kinetics of the 5TCX-AgCu nanocomposite were systematically investigated by varying the scan rate between 10 and 100 mV s⁻¹ in 0.1 M Na₂SO₄ electrolyte (pH 11.0), with 20 mM NO₃⁻ for the GCE-based system. The electrocatalytic behavior was evaluated by monitoring the current response associated with the irreversible reduction peak (E3) of NO₃⁻ and (E4) of NO₂⁻. A progressive increase in the I_{pc} was observed with increasing scan rates for both substrates, indicating enhanced electron transfer kinetics.

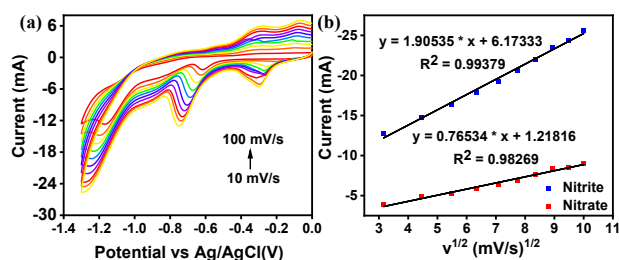


Figure 7: (a) CV profiles recorded in 0.1 M Na₂SO₄ (pH 11) containing 20 mM NO₃⁻ at varying scan rates (10-100 mV/s); (b) Linear dependence of peak current on the square root of scan rate for 5TCX-AgCu in the detection of NO₃⁻ and NO₂⁻.

Linear relationships were observed between I_{pc} and the scan rate (v), as shown in **Figure 7c, d** for the GCE configurations. The regression equations for NO₃⁻ and NO₂⁻ exhibited high correlation coefficients ($R^2 = 0.993$ and 0.982 , respectively), confirming the electrochemical stability and reproducibility of

the electrode system. Notably, the linearity between I_{pc} and v was superior to that between I_{pc} and the square root of v ($R^2 = 0.993$), indicating that the redox process is predominantly surface-controlled rather than diffusion-controlled. Since a slope of 0.5 typically characterizes a diffusion-limited process, the higher observed value strongly supports an adsorption-controlled mechanism for both NO₃⁻ and NO₂⁻ reduction at the SPCE/5TCX-AgCu and GCE/5TCX-AgCu interface. This behavior is attributed to the high surface area and electronic conductivity imparted by the bimetallic Cu-Ag decoration on the TCX framework, which promotes effective adsorption of NO₃⁻ and NO₂⁻ ions also facilitates their interaction with catalytically active sites. This interaction contributes to the enhanced redox current responses for both GCE/5TCX-AgCu and SPCE/5TCX-AgCu configurations.

To quantitatively assess the surface concentration (Γ) of electroactive sites, the Brown-Anson model was applied using the following equation:²⁹

$$I_{pc} = n^2 F^2 \Gamma \times A v / 4RT \quad (3)$$

Where I_{pc} is the cathodic peak current, Γ is the surface concentration, v is the scan rate (mV s⁻¹), A is the electrode surface area (SPCE = 0.1256 cm²), and n , F , R , and T represent their usual physical constants. Based on this model, the calculated Γ for SPCE/5TCX-AgCu was determined to be 0.5×10^{-6} mol cm⁻². These values indicate a high density of catalytically active sites, which significantly contribute to the observed electrocatalytic performance for NO₃⁻ and NO₂⁻ reduction.

3.2.4. Influence of Analyte Concentration

The electrocatalytic sensing performance of the 5TCX-AgCu nanocomposite was systematically investigated using two electrode platforms for NO₃⁻ detection: GCE (**Figure S3(b-d)**, **Figure S5(a-c)**) and SPCE (**Figure 8**). Electrochemical measurements were conducted over NO₃⁻ concentration ranges of 0.1-20 mM for GCE/5TCX-AgCu and 0.1-100 mM for SPCE/5TCX-AgCu. In both cases, the recorded electrochemical responses were attributable to the stepwise reduction of NO₃⁻ to NO₂⁻, followed by further reduction to NH₃, confirming a sequential and continuous electrochemical conversion pathway. For NO₂⁻ sensing, SPCE/5TCX-AgCu was evaluated across a concentration range of 0.1-30 mM, wherein the progressive increase in cathodic current corresponding to the reduction of NO₂⁻ to NH₃ validated its effective electrocatalytic activity.

Under optimized conditions, SWV was employed for the sensitive detection of NO₃⁻ using both electrode configurations and NO₂⁻ detection using SPCE only, as shown in **Figure S5a** (GCE) and **Figures 8a, c** (SPCE) for NO₃⁻, and **Figure 8e** for NO₂⁻. The SWV profiles exhibited well-defined, concentration-dependent cathodic peaks, confirming the reliable and responsive behavior of the modified electrodes toward NO₃⁻ and NO₂⁻ within the evaluated ranges.

The incremental enhancement in peak current with increasing NO₃⁻ concentration indicates effective surface activity and electrochemical affinity of the 5TCX-AgCu composite. **Figure 8(b, d)** presents the calibration plot correlating NO₃⁻ and NO₂⁻ concentration with the reduction peak current, which



demonstrates two distinct linear response regions for the SPCE/5TCX-AgCu sensor. For NO_3^- detection, within the lower concentration range (0.1-10 mM), the sensor demonstrated excellent linearity, yielding correlation coefficients of 0.987 for NO_3^- and 0.985 for NO_2^- . At higher concentrations (10-100 mM), the calibration plots continued to exhibit strong linear responses, with slightly improved correlation coefficients of 0.992 for NO_3^- and 0.994 for NO_2^- . For NO_2^- detection (Figure 8f), correlation coefficients of 0.990 in the lower range (0.1-1 mM) and 0.983 in the higher range (1-30 mM) were obtained, demonstrating the sensor's reliability across a broad dynamic window.

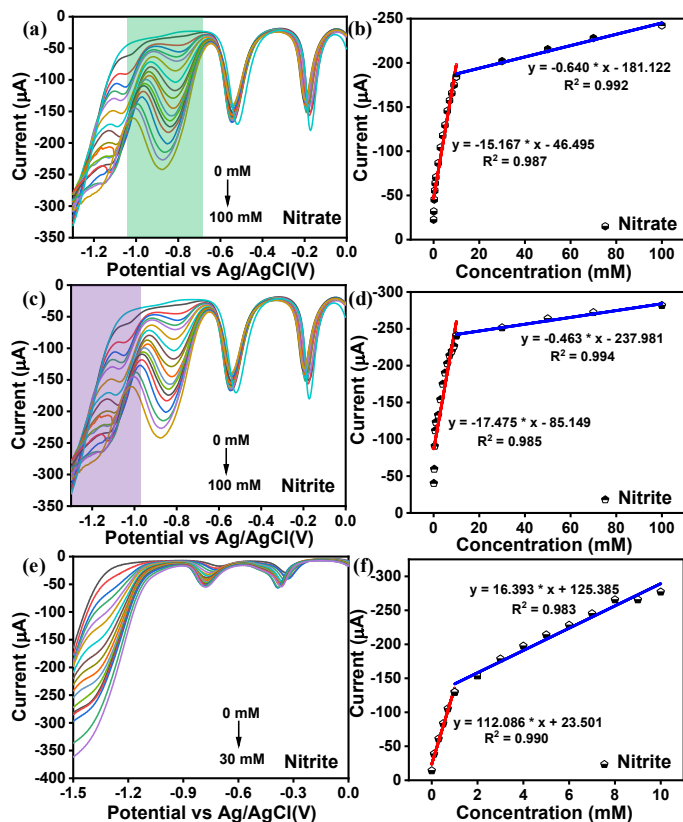
AgCu system was evaluated across two distinct ranges: 0-10 mM and 10-100 mM for NO_3^- (Table 1), 0.1 mM and 1-30 mM for NO_2^- (Table 2). Table S2 and Table S3 offers a comparative analysis of previously reported electrochemical NO_3^- and NO_2^- sensors based on various modified electrode configurations.^{11,31-44}

3.2.5. Interference Study

The ability to achieve selective detection is essential to validate the functionality of a sensor. In this study, the Potentiostatic method was conducted with the overpotential of -0.89V to evaluate the performance of SPCE for detecting NO_3^- and NO_2^- in the presence of potential interfering molecules (Figure S6a). The Potentiostatic method included CH_3COO^- , NH_4^+ , Fe^{2+} , Fe^{3+} , Mn^{2+} , and adding again NO_3^- and NO_2^- to observe if the material is still highly selective towards the target analyte in the presence of interference (Figure S6b).

3.2.6. Reproducibility, Repeatability, and Stability

To further assess the reproducibility of the electrode, repeated NO_3^- detection experiments were conducted using a single electrode subjected to successive measurements with increasing concentrations of NO_3^- . The resulting RSD of approximately 3.5% suggests a minor decline in current response, potentially due to surface saturation or partial fouling of the active sites. The repeatability of the SPCE/5TCX-AgCu sensor was evaluated using SWV across four independently fabricated electrodes under identical experimental conditions (Figure S7c, d). The calculated relative standard deviation (RSD) of 1.9% demonstrates excellent consistency in the electrochemical response among the different electrodes. Minor fluctuations in the reduction peak current were observed, which can likely be attributed to slight variations in manual electrode preparation and conduct. Moreover, the long-term electrochemical stability of the modified electrode was investigated by subjecting the modified electrode to 100 consecutive CV scans at a scan rate of 50 mV s^{-1} in 0.1 M Na_2SO_4 (pH 11.0) containing 20 mM NO_3^- , as demonstrated in (Figure S7a). The SWV responses recorded before and after CV cycling exhibited minimal changes, thereby confirming the robust stability of the electrode under continuous operation (Figure S7b). Collectively, the repeatability, reproducibility, and electrochemical stability assessments indicate that the SPCE/5TCX-AgCu sensor exhibits excellent reliability and is well-suited for practical applications in NO_3^- and NO_2^- detection.



The sensitivity and LOD³⁰ for both GCE/5TCX-AgCu and SPCE/5TCX-AgCu platforms were calculated using the standard analytical expressions, and the results are detailed in the subsequent section.

$$\text{LOD} = 3 \times \text{Standard deviation} / \text{Slope} \quad (4)$$

$$\text{Sensitivity} = \text{Calibration line slope} / \text{Surface area} \quad (5)$$

Using the equations outlined above, the LOD and sensitivities for NO_3^- and NO_2^- were evaluated for the GCE/5TCX-AgCu system within the 0.1-20 mM of NO_3^- concentration range employing CV and SWV techniques. Similarly, the SPCE/5TCX-

Figure 8: SWV of SPCE/5TCX-AgCu in 0.1 M Na_2SO_4 (pH 11.0) with linear range of (0.1, 0.3, 0.5, 0.7, 1, 2, 3, 4, 5, 6, 6, 7, 8, 9, 10, 30, 50, 70, 100 mM) of NO_3^- concentrations (a), (c); Linear relationship curve (b) NO_3^- , (d) NO_2^- ; (e) SWV of SPCE/5TCX-AgCu in 0.1 M Na_2SO_4 (pH 11.0). with the linear range of (0.1, 0.3, 0.5, 0.7, 1, 2, 3, 4, 5, 6, 7, 8, 9, 10, 20, 30 mM) of NO_2^- ion concentrations; (f) Linear relationship curve of NO_2^- .



Table 1: LOD and sensitivity of the GCE/5TCX-AgCu and SPCE/5TCX-AgCu for NO₃⁻ detection.

Substrate	Technique	Analyte Concentration (mM)	LOD (μM)		Sensitivity (μA mM ⁻¹ cm ⁻²)	
			NO ₃ ⁻	NO ₂ ⁻	NO ₃ ⁻	NO ₂ ⁻
GCE	CV	0 to 20	600	305.5	7	21
	SWV	0 to 20	84.7	52.8	10.1	16.6
SPCE	SWV	0 to 10	5.2	1.7	220.75	139.13
		10 to 100	124.0	64.0	5.095	3.68

Table 2: LOD and sensitivity of the SPCE/5TCX-AgCu for NO₂⁻ detection.

Substrate	Technique	Analyte Concentration (mM)	LOD (μM)	Sensitivity (μA mM ⁻¹ cm ⁻²)
SPCE	SWV	0 to 1	0.031	898.12
		1 to 10	0.211	131.35

3.2.7. Real Sample Analysis

The practical applicability of the SPCE/5TCX-AgCu based electrochemical sensor was evaluated through SWV for the detection of NO₃⁻ in real environmental water samples, including soil water, lake water, and tap water collected from Harohalli, India. Before analysis, the samples were centrifuged and filtered to remove particulate matter and suspended solids, ensuring matrix compatibility with electrochemical measurements. Preliminary analyses of the untreated water samples revealed no detectable levels of NO₃⁻ within the sensor's detection limit. To assess the sensor's quantitative performance in real matrices, known concentrations of NO₃⁻ were spiked into the pretreated soil, lake, and tap water samples (Pretreatment involved washing the soil sample with deionized water, followed by centrifugation of the resulting supernatant until residual soil particles were fully removed). The resulting data, summarized in (Table S4), demonstrate the sensor's ability to quantify NO₃⁻ concentrations across various water types accurately. The calculated recovery rates, ranging from 85.6% to 94.8%, reflect the high accuracy and reliability of the SPCE/5TCX-AgCu sensor in complex environmental samples. These conclusions affirm that the 5TCX-AgCu nanocomposite-modified electrode is a promising candidate for the development of practical electrochemical sensing platforms for NO₃⁻ and NO₂⁻ detection in real-world water sources.

4. Conclusions

The current study produced a straightforward, reusable, and simple electrochemical sensor based on a SPCE/5TCX-AgCu composite. The Cu and Ag NPs decorating the TCX surface are required to achieve the optimal sensing performance for the one-step dual detection of NO₃⁻ and NO₂⁻. Additionally, because soil has an alkaline pH system, a 0.1 M Na₂SO₄ solution at pH 11 was utilized as the electrolyte, allowing for the direct measurement of the NO₃⁻ concentration in soil samples. SEM, EIS, and SWV were employed to characterize the surface alteration, along with the analytical performance of the modified electrodes. The sensor's stability, repeatability,

selectivity, sensitivity, and reproducibility have all been established. The devised analytical method was successfully used to determine the amount of NO₃⁻ in soil and freshwater samples from actual environments. This sensing technology is a promising alternative approach for its integration into portable sensing platforms for NO₃⁻ detection in water because of its features, which include simplicity and speed of fabrication and analysis, as well as good performance and stability over time at room temperature. In future studies, we aim to extend the applicability of the 5TCX-AgCu sensor by performing high-performance liquid chromatography (HPLC) for rigorous validation with complex real samples. Additionally, long-term stability assessments under varied environmental conditions, miniaturization into portable sensing platforms, and exploration of multiplexed detection strategies will be pursued. These efforts will help translate the current proof-of-concept into robust, field-deployable devices for sustainable environmental and agricultural monitoring.

Conflicts of interest

The authors declare no conflict of interest.

Acknowledgements

The authors extend their appreciation for the financial assistance provided by the ANRF Core Research Grant (Grant No. CRG/2022/000897) and Jain University Grant (JU/MRP/CNMS/118/2025). C. S. R. acknowledges backing from the National Research Foundation of Korea under the Brain Pool program, funded by the Ministry of Science and ICT, South Korea (Grant No. RS-2023-00222186). The work is further supported by the National Research Foundation of Korea (NRF) funded by the Ministry of Science and ICT (Grant No. RS- 2023-00217581 and 2024-00345983).

Data Availability Statement

The accompanying author can provide the data supporting the study's conclusions upon reasonable request.

References

- 1 A. Du Plessis, *One Earth*, 2022, **5**, 129–131.
- 2 N. Jadon, H. K. Sharma, N. Gururibam and A. K. S. Chauhan, in *Current Directions in Water Scarcity Research*, eds. A. K. Tiwari, A. Kumar, A. K. Singh, T. N. Singh, E. Suozzi, G. Matta and S. Lo Russo, Elsevier, 2022, vol. 5, pp. 225–246.
- 3 M. Breida, S. A. Younssi, M. Ouammou, M. Bouhria, M. Hafsi, M. Breida, S. A. Younssi, M. Ouammou, M. Bouhria and M. Hafsi, in *Water Chemistry*, IntechOpen, 2019.
- 4 K. Ferysiuk and K. M. Wójciak, *Antioxidants*, 2020, **9**, 711.
- 5 A. Boink and G. Speijers, *Acta Hort.*, 2001, 29–36.
- 6 R. Cammack, C. L. Joannou, X.-Y. Cui, C. Torres Martinez, S. R. Maraj and M. N. Hughes, *Biochimica et Biophysica Acta (BBA) - Bioenergetics*, 1999, **1411**, 475–488.
- 7 L. Ma, L. Hu, X. Feng and S. Wang, *Aging Dis*, 2018, **9**, 938–945.
- 8 M. H. Ward, R. R. Jones, J. D. Brender, T. M. de Kok, P. J. Weyer, B. T. Nolan, C. M. Villanueva and S. G. van Breda, *Int J Environ Res Public Health*, 2018, **15**, 1557.
- 9 K. Pompapathi, K. S. Anantharaju, P. Karuppasamy, M. Subramaniam, B. Uma, S. Boppanahalli Siddegowda, A. Paul Chowdhury and H. C. A. Murthy, *ACS Environ Au*, 2024, **4**, 106–125.
- 10 P. Karuppasamy, N. Ramzan Nilofar Nisha, A. Pugazhendhi, S. Kandasamy and S. Pitchaimuthu, *Journal of Environmental Chemical Engineering*, 2021, **9**, 105254.
- 11 H. Bagheri, A. Hajian, M. Rezaei and A. Shirzadmehr, *Journal of Hazardous Materials*, 2017, **324**, 762–772.
- 12 A. K. M. S. Inam, M. A. Costa Angeli, B. Shkodra, A. Douaki, E. Avancini, L. Magagnin, L. Petti and P. Lugli, *ACS Omega*, 2021, **6**, 33523–33532.
- 13 A. Mahajan and M. Gupta, *Applied Organometallic Chemistry*, 2023, **37**, e7195.
- 14 S. Benhaiba, A. E. Attar, O. Salhi, B. Bouljoiel, C. Jama, S. Youssefi, A. Ezzahi and M. E. Rhazi, *Anal. Methods*, 2025, **17**, 5868–5885.
- 15 Md. A. Ali, Y. Jiao, S. Tabassum, Y. Wang, H. Jiang and L. Dong, in *2017 19th International Conference on Solid-State Sensors, Actuators and Microsystems (TRANSDUCERS)*, 2017, pp. 238–241.
- 16 J. Gajdár, S. Rodrigues Gaspar and M. G. Almeida, *TrAC Trends in Analytical Chemistry*, 2025, **183**, 118105.
- 17 J. Wei, Y. Li, H. Lin, X. Lu, C. Zhou and Y. Li, *Environmental Science and Ecotechnology*, 2024, **20**, 100383.
- 18 I. Sanchis, E. Diaz, A. H. Pizarro, J. J. Rodriguez and A. F. Mohedano, *Separation and Purification Technology*, 2022, **290**, 120750.
- 19 G. T. M. Kadja, S. A. C. Natalya, F. Balqis, N. J. Azhari, N. Nurdini, A. Sumboja, R. S. Rahayu, U. Pratomo, M. Khalil, and Irkham, *Nano-Structures and Nano-Objects*, DOI:10.1016/j.nanoso.2023.101059.
- 20 A. Aris, W. T. Wahyuni, B. R. Putra, A. Hermawan, F. A. A. Nugroho, Z. W. Seh and M. Khalil, *Nanoscale*, 2025, **17**, 2554–2566.
- 21 R. Hasanah, Y. Romdoni, V. Fauzia, A. Arifutzzaman, F. Hussin, M. K. Aroua and M. Khalil, *Materials Research Bulletin*, DOI:10.1016/j.materresbull.2025.113514.
- 22 I. Sterin, A. Tverdokhlebova, O. Smutok and E. Katz, *J Solid State Electrochem*, 2024, **28**, 757–827. DOI: 10.1039/D5SD00187K
- 23 C. B. Cockreham, V. G. Goncharov, E. Hammond-Pereira, M. E. Reece, A. C. Strzelecki, W. Xu, S. R. Saunders, H. Xu, X. Guo and D. Wu, *ACS Appl. Mater. Interfaces*, 2022, **14**, 41542–41554.
- 24 B. Kui, S. Zhao, Y. Hu, K. Zheng, Y. Yao, S. Chen, N. Wang, P. Gao, Z. Bai and W. Ye, *Catal. Sci. Technol.*, 2025, **15**, 1617–1626.
- 25 V. Colic, M. D. Pohl, D. Scieszka and A. S. Bandarenka, *Catalysis Today*, 2016, **262**, 24–35.
- 26 P. Guo, K. Liu, X. Liu, R. Liu and Z. Yin, *Energy Fuels*, 2024, **38**, 5659–5675.
- 27 W. Liao, J. Wang, G. Ni, K. Liu, C. Liu, S. Chen, Q. Wang, Y. Chen, T. Luo, X. Wang, Y. Wang, W. Li, T.-S. Chan, C. Ma, H. Li, Y. Liang, W. Liu, J. Fu, B. Xi and M. Liu, *Nat Commun*, 2024, **15**, 1264.
- 28 E. P. Randviir, *Electrochimica Acta*, 2018, **286**, 179–186.
- 29 P. Zhu and Y. Zhao, *Materials Chemistry and Physics*, 2019, **233**, 60–67.
- 30 B. Kulkarni, V. Suvina, K. Pramoda and R. G. Balakrishna, *Journal of Electroanalytical Chemistry*, 2023, **931**, 117175.
- 31 M. Atmeh and B. E. Alcock-Earley, *J Appl Electrochem*, 2011, **41**, 1341–1347.
- 32 G. Khadige, .
- 33 K. Fajerwerger, V. Ynam, B. Chaudret, V. Garçon, D. Thouron and M. Comtat, *Electrochemistry Communications*, 2010, **12**, 1439–1441.
- 34 D. Chen Legrand, C. Barus and V. Garçon, *Electroanalysis*, 2017, **29**, 2882–2887.
- 35 S. Zhao, J. Tong, Y. Li, J. Sun, C. Bian and S. Xia, *Micromachines*, 2019, **10**, 223.
- 36 T. Öznülür, B. Özdurak and H. Öztürk Doğan, *Journal of Electroanalytical Chemistry*, 2013, **699**, 1–5.
- 37 N. Comisso, S. Cattarin, P. Guerriero, L. Mattarozzi, M. Musiani, L. Vázquez-Gómez and E. Verlato, *J Solid State Electrochem*, 2016, **20**, 1139–1148.
- 38 M.-C. Tsai, D.-X. Zhuang and P.-Y. Chen, *Electrochimica Acta*, 2010, **55**, 1019–1027.
- 39 S. M. Shariar and T. Hinoue, *ANAL. SCI.*, 2010, **26**, 1173–1179.
- 40 M. Ammam, B. Keita, L. Nadjo and J. Fransaer, *Talanta*, 2010, **80**, 2132–2140.
- 41 Z. Zhang, G. Ogata, K. Asai, T. Yamamoto and Y. Einaga, *ACS Sens.*, 2023, **8**, 4245–4252.
- 42 L. A. Pradela-Filho, B. C. Oliveira, R. M. Takeuchi and A. L. Santos, *Electrochimica Acta*, 2015, **180**, 939–946.
- 43 R. Hallaj, A. Salimi, B. Kavosi and G. Mansouri, *Sensors and Actuators B: Chemical*, 2016, **233**, 107–119.
- 44 R. Yu, L. Wang, Q. Xie and S. Yao, *Electroanalysis*, 2010, **22**, 2856–2861.



Data Availability Statement

The accompanying author can provide the data supporting the study's conclusions upon reasonable request.

